

Auto-ejection of liquid drops from capillary tubes

Hadi Mehrabian¹ and James J. Feng^{1,2,†}

¹Department of Chemical and Biological Engineering, University of British Columbia, Vancouver, BC V6T 1Z3, Canada

²Department of Mathematics, University of British Columbia, Vancouver, BC V6T 1Z2, Canada

(Received 2 January 2014; revised 5 May 2014; accepted 17 June 2014)

Wicking flow inside capillary tubes can attain considerable momentum so as to produce a liquid jet at the end of the tube. Auto-ejection refers to the formation of droplets at the tip of such a jet. Experimental observations suggest that a tapering nozzle at the end of the capillary tube is necessary for auto-ejection; it has never been reported for a straight tube. Besides, most experimental realizations require microgravity, although it is possible under normal gravity if the nozzle has a sufficiently sharp contraction. This computational study focuses on two related issues: the critical condition for auto-ejection, and the hydrodynamics of the liquid meniscus as affected by geometric parameters. We adopt a diffuse-interface Cahn–Hilliard model for the moving contact line, and allow the dynamic contact angle to deviate from the static one through wall energy relaxation. From analyzing the dynamics of the meniscus in the straight tube and the nozzle, we establish a critical condition for the onset of auto-ejection based on a Weber number defined at the exit of the nozzle and an effective length that encompasses the geometric features of the tube–nozzle combination. In particular, this shows that capillary ejection is not possible in straight tubes. With steeper contraction in the nozzle, we predict two additional regimes of interfacial rupture: rapid ejection of multiple droplets and air bubble entrapment. The numerical results are in general agreement with available experiments.

Key words: capillary flows, contact lines, drops and bubbles

1. Introduction

Droplet production is a fluid dynamical process of considerable importance in engineering applications. The rapid development of microfluidic technology has given new impetus to the study of controlled drop production in miniaturized devices (Goldmann & Gonzalez 2000). A common method for drop production is to pump liquid through a tube such that a jet issues from the end, and breaks up due to capillary instability. In microfluidics, this is typically realized by flow focusing (Anna, Bontoux & Stone 2003; Takeuchi *et al.* 2005), and two regimes, jetting and dripping, have been identified (Ambravaneswaran *et al.* 2004; Utada *et al.* 2005; Zhou, Yue & Feng 2006). Jet breakup can be actively promoted and controlled by a pressure pulse,

† Email address for correspondence: jfeng@chbe.ubc.ca



FIGURE 1. (Colour online) A sequence of snapshots showing spontaneous capillary rise and auto-ejection of droplets in the experiment of Wollman & Weislogel (2013) under microgravity. The inner diameter of the glass tube is 9.2 mm in the straight section, and the liquid is PDMS of viscosity 0.65 cs. The drop volume is roughly 20 μl . The photos are taken 0.1 s apart. Adapted from Wollman & Weislogel (2013) with permission, ©Springer.

as in drop-on-demand devices (Xu & Basaran 2007; Basaran & Xu 2012; Basaran, Gao & Bhat 2013). In these schemes of drop formation, the jet is always fed by an externally controlled flow rate.

Recently, Wollman and coworkers have demonstrated a novel method of drop formation that relies on wicking in a capillary tube (Wollman 2012; Wollman *et al.* 2012; Wollman & Weislogel 2013). As shown in figure 1, a glass tube with a tapered end is put into contact with a reservoir of silicone oil, which wets the glass perfectly. The liquid meniscus rises with sufficient momentum such that a jet is ejected from the nozzle, and later disintegrates into droplets. The sequence of photos shown here was captured under microgravity in a drop tower (Wollman & Weislogel 2013). Similar experiments have been done in the International Space Station and under normal gravity on Earth (Wollman 2012; Wollman *et al.* 2012). The process is interesting in that it involves no external force or flux, and is entirely autonomous. Wollman & Weislogel (2013) called it auto-ejection.

Two interesting questions can be asked about this process: what the critical condition is for ejecting one or more drops, and how geometric parameters of the problem affect the ejection. The ejection process is governed by inertia as well as capillarity, much like for Worthington jets (Gekle & Gordillo 2010) and cavity jets (Antkowiak *et al.* 2007). Regarding the first question, it seems reasonable to argue that auto-ejection occurs when the upward momentum of the liquid column overcomes its surface tension. As will be shown later, viscous friction is negligible under typical experimental conditions. However, it is difficult to quantify this idea in terms of a Weber number. This is because both the liquid momentum and the capillary restriction vary in time as complex functions of several factors, including the dynamic contact angle, the shape of the nozzle and contact-line pinning. In

particular, auto-ejection has never been recorded at the end of a straight tube; the converging nozzle seems to be necessary (Siegel 1961; Wollman & Weislogel 2013). Wollman & Weislogel (2013) devised a semi-empirical expression for a modified Weber number, and showed that a threshold in this number corresponds roughly with the onset of auto-ejection. But there is considerable scatter in the data.

To analyse this intricate process, it seems appropriate to divide it into two stages: the acceleration of the meniscus inside the tube, including the nozzle at the end, and the protrusion and possible breakup of the jet outside the nozzle. In the following, we will briefly summarize the current state of knowledge on each phenomenon.

Capillary rise inside straight tubes has been extensively studied before (e.g. Lowndes 1980). Depending on which resistive force counteracts the capillary driving force, three regimes may be delineated (Stange, Dreyer & Rath 2003). After the initial transient of meniscus formation, an inertial regime follows in which the rise velocity increases with the meniscus height and with time. Then comes a regime dominated by the convective pressure loss in the liquid reservoir and the capillary tube, with a constant rise velocity (Quéré, Raphaël & Ollitrault 1999; Stange *et al.* 2003):

$$v_{ci} = \left(\frac{2\sigma \cos \theta_d}{\rho R} \right)^{1/2}, \quad (1.1)$$

where R is the tube radius, ρ is the liquid density, σ is the surface tension and θ_d is the dynamic contact angle. This is known as the capillary–inertial velocity. As the imbibition proceeds, the liquid column increases in length and mass. Viscous friction becomes important and the meniscus velocity starts to decline. Eventually inertia becomes unimportant and the dynamics enters the Lucas–Washburn regime where capillary pressure balances the viscous friction (Lucas 1918; Washburn 1921). Denoting the liquid viscosity by μ , we can write the velocity of rise as

$$v_{LW} = \frac{R\sigma \cos \theta_d}{4\mu H}, \quad (1.2)$$

which decreases with the length of the liquid column H . In the auto-ejection process, however, it is not clear *a priori* if the meniscus velocity follows any of these scalings. What is more, these simple models disregard the contact-line dynamics (Huh & Scriven 1971). At high velocities, the dynamic contact angle θ_d may deviate considerably from the static one θ (Hoffman 1975; Bracke, De Voeght & Joos 1989). Thus, the capillary force driving the meniscus changes with its velocity, adding another subtlety to the problem.

As the nozzle is essential for auto-ejection, the meniscus acceleration inside the nozzle is a key aspect of the process. For inertialess flows, Mehrabian & Feng (2011) have investigated the meniscus dynamics inside contractions, including the transient turning of the interface, its evolving curvature as well as the overall acceleration of the liquid column. Auto-ejection requires a high incoming momentum with a large inertia, and the meniscus dynamics inside the nozzle remains to be studied.

In the second stage of auto-ejection, a jet emanates from the nozzle, and one or more droplets form at the tip, apparently through a capillary mechanism known as end-pinching (Stone & Leal 1989). Essentially, capillary retraction at the tip produces a bulbous end, whose neck then becomes susceptible to capillary pinch-off. End-pinching has been studied by linear instability analysis (Leib & Goldstein 1986), a one-dimensional lubrication model (Ambravaneswaran, Wilkes & Basaran 2002),

experiments (Umemura 2011; Castrejón-Pita *et al.* 2012a) and numerical simulations (Schulkes 1996; Ha & Leal 2001; Notz & Basaran 2004; Tong & Wang 2007). These studies have assumed either zero incoming flow at the base of the jet or a constant flow rate. The auto-ejection problem differs in that the jet is being fed by a time-dependent flow rate that is governed by the morphology of the jet and the physical conditions inside the tube and nozzle. Thus, spatial and temporal variations of the liquid velocity determine the fate of the jet and the number and size of any droplets that may form. In this regard, auto-ejection resembles the drop-on-demand inkjet printing process, where a pressure pulse upstream of the nozzle modulates the flow rate and promotes drop ejection (Chen & Basaran 2002; Dong, Carr & Morris 2006; Basaran *et al.* 2013). The process is sometimes modelled by imposing a flow rate that varies sinusoidally in time (Xu & Basaran 2007; Basaran & Xu 2012). Besides, Gordillo & Gekle (2010) have used a linearly decreasing incoming velocity to study Worthington jets. Prior studies have indicated additional geometric complications related to the shape and wettability of the lip of the nozzle (Ambravaneswaran *et al.* 2004). How the interface may de-pin from the inner edge of the lip and move along its width turns out to have a strong influence on drop pinch-off.

The review of prior work suggests the criterion for auto-ejection to be the most prominent question. Ideally, the criterion should predict how auto-ejection depends on geometric factors: tube length, contraction angle, and even the width of the lip at the exit of the nozzle. To develop such a criterion, one must study the meniscus dynamics in the tube and the nozzle, as well as the jet behaviour outside. We undertake such an investigation using numerical simulations that capture detailed features of the contact-line dynamics. As will be explained in §4.2, the numerical results suggest critical conditions based on the instantaneous liquid velocity when the jet exits the nozzle, but not a criterion in terms of the tube and nozzle geometry.

2. Problem set-up

The axisymmetric geometry of the problem consists of a capillary tube connected to a liquid reservoir at the bottom and ambient air at the top (figure 2). In most of the simulations the tube has a contracting nozzle at its upper end. The contraction angle is α and the radius shrinks from the tube radius R to R_n at the end of the nozzle. The total length of the tube, including the nozzle, is L . Thus, the flow geometry is specified by three dimensionless quantities: the contraction angle α , the contraction ratio $C = R_n/R$ and the aspect ratio L/R . Initially the air–liquid interface is assumed flat at a small distance L_0 inside the tube. For the most part, L_0 represents the capillary climb under normal gravity before the drop-tower experiment commences (Wollman & Weislogel 2013). There is also a numerical incentive for placing the interface inside the tube to avoid complications at the corner.

The liquid and air reservoirs are sufficiently large that their boundaries have no effect on dynamics of the meniscus, liquid jet and drops. Based on numerical experiments, we have chosen the liquid reservoir to be $3R$ in radius and $4R$ in height. On its bottom and side walls, we impose zero normal stress and zero tangential velocity as boundary conditions. Its top wall is taken to have zero shear stress and zero normal velocity. This boundary condition avoids the computational cost of tracking the slight deformation of the liquid–air interface outside the tube. Stange *et al.* (2003) have shown that this simplification has little effect on the meniscus motion, and we have reached the same conclusion by benchmarking our simulation of capillary rise against experiments. The air reservoir on top is $4R_n$ in radius, and

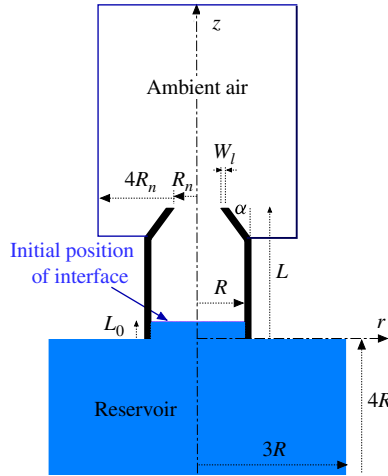


FIGURE 2. (Colour online) Schematic of the meridian plane of the axisymmetric computational domain, not drawn to scale.

its height ranges from $12R_n$ to $30R_n$ depending on the length of the jet in different simulations. Zero stress boundary conditions are used on the top, bottom and sides of the air reservoir. On the sloping walls of the nozzle, no-slip conditions are imposed. The upper surface of the nozzle (or the ‘lip’) is a horizontal ring of width W_l . For most of the simulations, this surface is assigned a contact angle $\theta_l = 180^\circ$ to ensure that the contact line remains pinned at the inner corner of the lip. Smaller θ_l values are used in § 4.4 to explore de-pinning of the interface from the sharp corner, which is known to occur in experiments (Wollman *et al.* 2012).

In addition to the geometric ratios, the problem is characterized by four dimensionless groups based on material properties: the liquid–air density ratio ρ/ρ_a and viscosity ratio μ/μ_a , the Ohnesorge number $Oh = \mu/\sqrt{\rho R \sigma}$, and the static contact angle θ inside the tube and nozzle. On the inner surface of the tube, we impose the no-slip condition, and model the motion of the three-phase contact line by Cahn–Hilliard diffusion to be discussed below. Gravity is neglected in all presented results except figure 10. This is because most of the experimental data have been collected under microgravity, and gravity tends to inhibit auto-ejection. We will fix these parameters: $\theta = 0^\circ$ (perfect wetting), $\rho/\rho_a = 200$ and $\mu/\mu_a = 100$. In comparison with the silicone oils used in the experiments (Wollman & Weislogel 2013), the density ratio is too low but the viscosity ratio is within the range of experimental values. In view of the numerical difficulties in computing larger density ratios, we are satisfied that the air has little influence on the liquid jet and drops at $\rho/\rho_a = 200$ (Gao & Feng 2011). We will vary the three geometric ratios C , α and L/R along with the Ohnesorge number Oh . We will use R as the characteristic length, the capillary–inertial time $t_{ci} = \sqrt{\rho R^3/\sigma}$ as the characteristic time, and R/t_{ci} as the characteristic velocity, and present the results in dimensionless form.

3. Physical model and numerical algorithm

From a computational viewpoint, the auto-ejection process is difficult to simulate as the interface moves, deforms and eventually breaks up, and the process features

a prominent role for the moving contact line. We adopt the Cahn–Hilliard model for this task, which regularizes the interfacial discontinuity by a diffuse interface and the stress singularity at the moving contact line by interfacial diffusion (Qian, Wang & Sheng 2006; Yue, Zhou & Feng 2010; Zhou *et al.* 2010; Yue & Feng 2011*a,b*; Sibley, Nold & Kalliadasis 2013; Sui, Ding & Spelt 2014). Thus, interfacial breakup and contact-line motion can be simulated naturally. The Cahn–Hilliard model represents the dynamics of the interface by a convection–diffusion equation in terms of a phase-field variable ϕ ,

$$\frac{\partial \phi}{\partial t} + \mathbf{v} \cdot \nabla \phi = \nabla \cdot (\gamma \nabla G), \quad (3.1)$$

where $\phi = \pm 1$ inside the liquid and air bulk phases, and $\phi = 0$ marks the interface. The mobility parameter γ is assumed to be constant, and the chemical potential

$$G = -\lambda \nabla^2 \phi + \frac{\lambda}{\epsilon^2} \phi (\phi^2 - 1) \quad (3.2)$$

follows from a Ginzburg–Landau free energy with a double-well potential, with ϵ being the interfacial thickness and λ the mixing energy density. To solve this equation along with the continuity and momentum equations, we pose the following boundary conditions on the solid walls:

$$\mathbf{v} = 0, \quad (3.3)$$

$$\mathbf{n} \cdot \nabla G = 0, \quad (3.4)$$

$$\mathbf{n} \cdot \nabla \phi = -\frac{f'_w(\phi)}{\lambda} - \frac{1}{\Gamma \lambda} \left(\frac{\partial \phi}{\partial t} + \mathbf{v} \cdot \nabla \phi \right), \quad (3.5)$$

where the normal vector \mathbf{n} points into the solid wall. Equation (3.3) is the no-slip condition on the wall, (3.4) dictates zero flux through it, and (3.5) comes from the variation of the wall energy $f_w = \phi(\phi^2 - 3)\sigma \cos \theta/4 + (\sigma_a + \sigma_l)/2$, Γ being the rate of wall energy relaxation (Jacquemin 2000; Qian *et al.* 2006; Yue & Feng 2011*a*). Note that f_w specifies the static contact angle θ through Young's equation $\sigma_a - \sigma_l = \sigma \cos \theta$, where σ_a and σ_l are the wall–fluid interfacial tension for the air and liquid. Therefore, our diffuse-interface model introduces four parameters: ϵ , λ , γ and Γ . The first two are constrained by the need to produce a prescribed interfacial tension: $\sigma = (2\sqrt{2}/3)(\lambda/\epsilon)$. That leaves us with three new model parameters, say ϵ , γ and Γ .

The choice of these parameters is informed by their physical meanings and the requirement of achieving the sharp-interface limit (Yue *et al.* 2010; Sibley *et al.* 2013). For example, γ gives a ‘diffusion length’ $l_d = (\mu\gamma)^{1/2}$ that is the counterpart of the slip length in sharp-interface models. Detailed discussions can be found in earlier papers (Yue & Feng 2011*a,b*), which recommend the following procedure. Choose as small an ϵ value as computationally affordable, and then pick a value for γ to ensure the sharp-interface limit being achieved. Finally, determine the wall relaxation parameter Γ by fitting an experimental datum.

To implement this procedure, we make the parameters dimensionless using a characteristic length l : $Cn = \epsilon/l$, $S = l_d/l$, and $\Pi = 1/(\Gamma\mu l)$. Here Cn is commonly known as the Cahn number (Zhou *et al.* 2010). One needs to be careful in choosing l . Accurate simulation using the diffuse-interface model requires that the interfacial thickness ϵ and the diffusion length l_d both be much smaller than the global length scale (Yue & Feng 2011*a*). As the meniscus advances through the nozzle, the effective

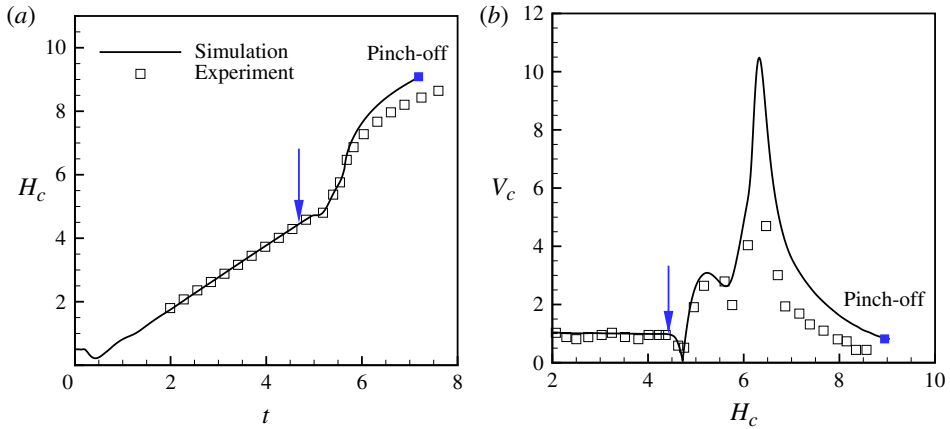


FIGURE 3. (Colour online) With a wall relaxation parameter $\Pi = 0.4$, the simulation approximates experimental results closely in terms of (a) the position of the centre of the meniscus, and (b) the centreline velocity of the meniscus. The arrows indicate the moment when the contact line reaches the start of the nozzle, and the curves end when a drop pinches off, indicated by a filled square. The geometric and physical parameters match the experiment of Wollman (2012): $Oh = 0.011$, $L = 5.98$, $C = 0.493$, $\alpha = 23.8^\circ$ and $\theta = 0^\circ$. In addition, $S = 8 \times 10^{-3}$ and $C_n = 0.01$.

global length scale is shrinking. We find it necessary to reduce ϵ and l_d accordingly to maintain accuracy of the simulation. Therefore, when the contact line is in the straight portion of the tube, we take $l = R$. When it is in the nozzle, we take l to be the local radius of the nozzle at the contact line. After the contact line reaches the lip, we fix $l = R_n$. Thus, with fixed values of C_n , S and Π , the microscopic lengths ϵ and l_d shrink inside the nozzle as required. Following Yue & Feng (2011b), we choose a small Cahn number $C_n = 10^{-2}$ that is comfortably computable, and a corresponding $S = 8 \times 10^{-3}$. Then we found that $\Pi = 0.4$ gives the closest agreement with the experimental results. This is illustrated in figure 3 in terms of the position and velocity of the centre of the meniscus.

The geometric and material parameters are chosen based on the experiment of Wollman *et al.* (2012). For direct comparisons, e.g. in figure 3, these are matched exactly with the experimental parameters: $Oh = 0.011$, $L = 5.98$, $C = 0.493$, $\alpha = 23.8^\circ$, static contact angle $\theta = 0^\circ$ inside the tube, and the initial height of the liquid column $L_0 = 0.08L$. We have also varied some of the parameters from this ‘baseline’ in later explorations, and their values will be specified in each case.

A notable feature of this simulation is the evolution of the dynamic contact angle θ_d . The wall energy relaxation in (3.5) allows θ_d to deviate from θ (Yue & Feng 2011b). Figure 4 compares our computed θ_d for capillary rise in a straight tube with two experimental correlations. In our computation, the meniscus rises with an essentially constant speed V , with which we define a capillary number $Ca = \mu V / \sigma$. The correlation of Bracke *et al.* (1989) is for θ_d on solid strips drawn into a pool of liquid, while that of Jiang, Soo-Gun & Slattery (1979) is based on the experiments of Hoffman (1975) on pushing non-polar liquids through glass capillary tubes. The numerical and experimental results all indicate an increase of θ_d with Ca , but the former exhibits a somewhat steeper slope than the experiments. One reason for the difference is that the Cahn–Hilliard model is phenomenological, and the mechanism

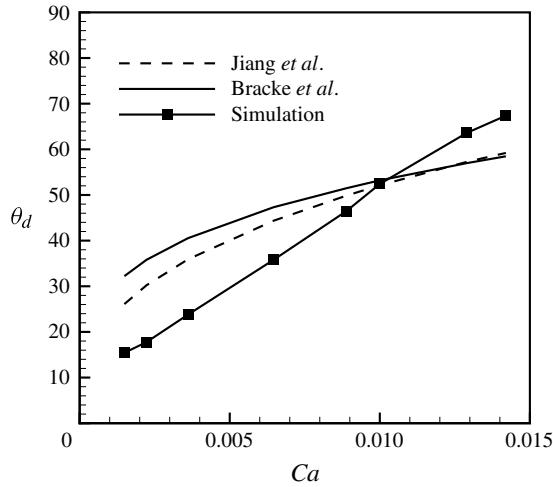


FIGURE 4. Comparison of the dynamic contact angle θ_d (in degrees) in a straight tube between our numerical simulation and two experimental correlations due to Jiang *et al.* (1979) and Bracke *et al.* (1989). The model parameters are the same as in figure 3.

of wall energy relaxation cannot be expected to capture quantitatively the dynamic contact angle. Moreover, the dynamic contact angle is known to depend on the outer flow geometry (Marsh, Garoff & Dussan 1993). Finally, in our simulations θ_d is measured from the slope of the interface where it intersects the wall. In the experiments, it is estimated from fitting a circular arc to the central portion of the meniscus. This introduces some discrepancy as well.

4. Results

4.1. Meniscus dynamics

We begin with an overview of the dynamics of the meniscus as it advances through the straight portion of the tube and the contracting nozzle, and forms a jet outside the nozzle. For this purpose we select a typical set of physical and geometric parameters: $Oh = 0.01$, $L = 5$, $C = 0.5$, $\alpha = 30^\circ$ and $\theta = 0^\circ$. To describe the motion and deformation of the meniscus, we track the contact-line velocity along the wall V_w and the velocity at the centre of the meniscus V_c in time.

Figure 5(a) plots V_w and V_c as functions of time. From an initially flat shape (figure 2), the meniscus experiences an acceleration and adjustment phase at the start of the imbibition. The contact line immediately moves upward at a roughly constant speed, while the centre of the meniscus oscillates several times before settling into a steady shape and speed of rise (point *a* in figure 5). This marks the start of the capillary–inertial regime. The meniscus velocity $V_w = V_c = 1.09$ agrees closely with the theoretical result $v_{ci} = 1.07$ (cf. (1.1)). This steady rise persists until point *b*, when the contact line arrives at the start of the nozzle. It is remarkable that the meniscus velocity stays roughly constant so far, showing little decrease due to viscous dissipation. This can be rationalized by an estimation of the viscous effect in a straight tube. By balancing the capillary, viscous and inertial forces, Bosanquet (1923) derived an analytical solution for the rise of the meniscus. For short times ($Oh t \ll 1$), this solution predicts the following variation of the meniscus velocity V_c

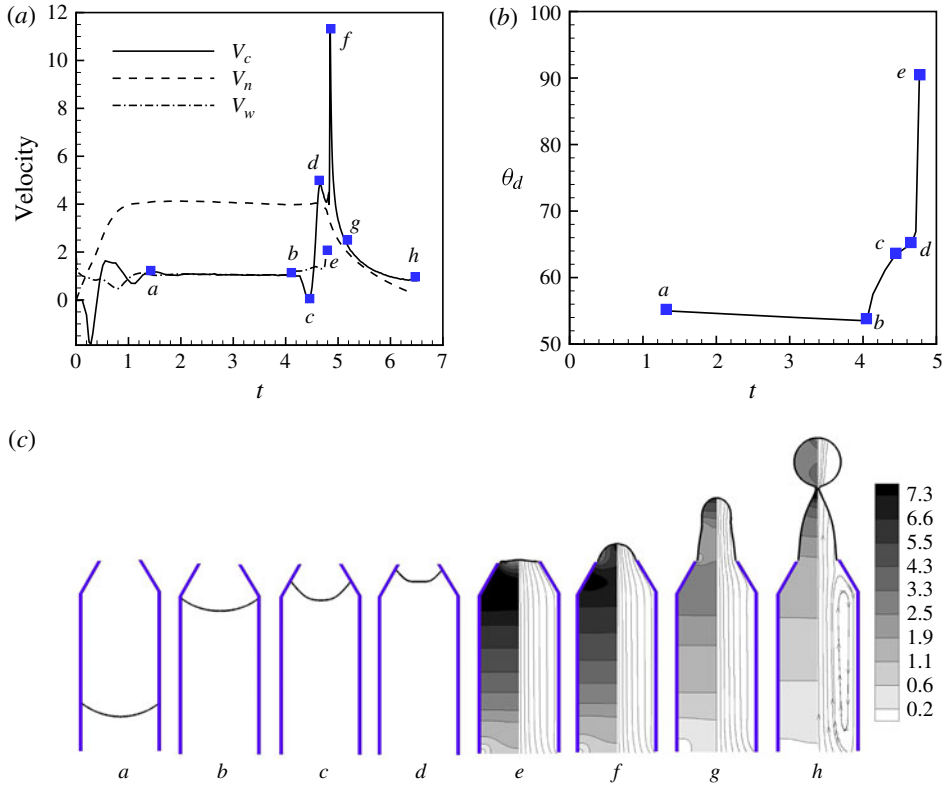


FIGURE 5. (Colour online) (a) Temporal evolution of the contact-line velocity V_w , meniscus centre velocity V_c , and average velocity at nozzle exit V_n . (b) Temporal evolution of the dynamic contact angle θ_d . (c) Snapshots showing the position and shape of the meniscus at significant moments marked in the velocity plot. The last four snapshots also show the pressure contours (left half) and streamlines (right half). $Oh = 0.01$, $\theta = 0^\circ$, $L = 5$, $C = 0.5$ and $\alpha = 30^\circ$.

with the meniscus height H_c :

$$\frac{1}{V_c} \frac{dV_c}{dH_c} = 2.4 Oh, \quad (4.1)$$

where V_c and H_c are dimensionless. Our numerical simulation verifies the proportionality to Oh , but with a milder slope of 1.8. For $Oh = 0.01$ and an axial distance of approximately 2.5 for the capillary–inertial regime in figure 5, therefore, viscous reduction of the meniscus velocity V_c is only approximately 5%. In fact, viscosity never plays an appreciable role throughout the entire process, and will be disregarded for the rest of the paper. In the experiments, Oh is typically of the order of 0.01 (Wollman & Weislogel 2013), and viscosity is generally immaterial.

Once the contact line reaches the nozzle, the interface immediately rotates, as if hinged at the contact line, so as to adjust its orientation relative to the tapering wall of the nozzle. This perturbation generates a capillary wave that propagates radially inward, and pushes the central portion of the meniscus backward by capillarity, thus reducing the centreline velocity V_c to a minimum at point c in figure 5(a). Afterwards,

the meniscus accelerates rapidly upward, mainly because of the momentum of the liquid column being channelled through a narrowing conduit. Capillarity also contributes to the acceleration since the meniscus is trailing the spherical shape at the moment, having been delayed by the rotation of the interface from b to c . This is illustrated in the snapshots of the interface in figure 5(c). This stage continues until point d , when the acceleration has moved the central portion of the meniscus ahead of the spherical surface dictated by the local dynamic contact angle. Thus capillary forces now pull the meniscus backward, causing the reduction in V_c until point e , when the contact line reaches the lip of the exit. Note that between points b and e , the contact-line speed V_w is still measured by the axial position of the contact line, not by the distance travelled along the wall. Figure 5(b) shows that the dynamic contact angle θ_d closely tracks the evolution of the contact-line speed V_w , in accordance with the observations in figure 4.

At point e , the contact line becomes pinned at the sharp inner corner of the lip according to Gibbs' criterion (e.g. Gao & Feng 2009). This constrains the upward flow near the nozzle wall and produces a high pressure behind the meniscus that thrusts the central portion of the meniscus out in the form of a jet (point f). Following Xu & Basaran (2007), we have plotted pressure contours and streamlines in the left and right halves of the meridian plane in figure 5(c). The disturbance at the bottom of the tube is due to proximity to the entrance of the capillary. As the jet is ejected and lengthens against surface tension, its tip velocity declines toward point g , when capillary necking commences on the jet, eventually leading to a droplet pinching off at the tip (point h). Note the high pressure at the neck due to the azimuthal curvature.

As depicted in figure 5, auto-ejection resembles ejection at the tip of oscillating pendant drops (Wilkes & Basaran 2001) and drop-on-demand inkjet printing (Chen & Basaran 2002; Dong *et al.* 2006). In the latter case, an upstream pressure pulse is applied to eject a drop at a nozzle. Once a liquid filament is produced outside the nozzle, drops may form at its tip by end-pinching (Dong *et al.* 2006), much as in auto-ejection. However, significant differences can be observed as well. In the experiment of Dong *et al.* (2006), the pressure pulse can produce a rather long filament that is susceptible to Rayleigh breakup. In the set-ups of Chen & Basaran (2002) and Xu & Basaran (2007) for producing small droplets, the meniscus is controlled by alternating forward and backward flows, and the base of the jet may retreat considerably into the nozzle. These features are absent in auto-ejection.

Figure 5(a) also plots the temporal evolution of V_n , the average velocity across the nozzle exit, for its importance in constructing an ejection criterion in the next subsection. Before the liquid meniscus arrives at the nozzle exit, V_n is computed from the velocity profile of air. It is interesting to contrast the behaviour of V_n with that of the meniscus velocity V_c . Note that thanks to incompressibility, V_n gives the average liquid velocity in the tube (subject to a factor C^2 due to area contraction), even before the meniscus reaches the lip of the nozzle. During the initial acceleration of the meniscus, prior to point a , V_n monotonically increases to a constant level that corresponds to the capillary–inertial regime. It starts to decline at point d , when capillarity starts to oppose the upward motion of the liquid. The decline continues monotonically even as the jet rapidly issues from the nozzle. This can be rationalized from how the interfacial tension, acting on the pinned contact line, continually depletes the upward momentum of the liquid column.

The decline of $V_n(t)$ in time after the jet formation (roughly from point f onward) can be quantified from an energy argument. Consider a control volume that encloses the inside of the tube and the nozzle, as well as the liquid reservoir. The kinetic energy

of the liquid inside, E , decreases because of the energy efflux at the nozzle as well as the pressure work there:

$$\frac{dE}{dt} = -\frac{1}{2}\pi R_n^2 \rho V_n^3 - p_n \pi R_n^2 V_n, \quad (4.2)$$

where p_n is the liquid pressure at the exit of the nozzle. Note that the pressure in the reservoir equals that in the ambient air, and has been put to zero, and that the energy influx at the boundary of the reservoir has been neglected as the velocity there is much smaller than that inside the capillary tube. Viscous dissipation is negligible as noted before. Here E is the sum of the kinetic energy in the tube, the nozzle and the reservoir. To estimate the fluid velocity inside the nozzle, we assume one-dimensional plug flow with a velocity that varies from V_n at the nozzle exit to $C^2 V_n$ inside the capillary tube. Similarly, the flow in the reservoir is assumed to be radial and uniform on spherical surfaces centred at the entry of the tube, with a velocity that can be related to V_n through mass conservation (Szekely, Neumann & Chuang 1971). Thus, E can be expressed in terms of V_n : $E \approx (\pi/2)\rho R_n^2 L_e V_n^2$, where the effective length

$$L_e = RC \frac{(1-C)^2}{\tan \alpha} + \left(L + \frac{7}{6}R\right) C^2 \quad (4.3)$$

is a purely geometric parameter. To estimate the exit pressure p_n , we note that the capillary pressure decreases from $2\sigma/R_n$ to σ/R_n as the liquid interface inflates from a semi-spherical shape to a cylinder with radius R_n . Taking $p_n = 2\sigma/R_n$, plugging E into (4.2) and integrating in time, we obtain

$$V_n(t) = u \tan \left[-\frac{u(t-t_f)}{2L_e} + \tan^{-1} \left(\frac{V_f}{u} \right) \right] = V_f \frac{1 - \frac{u}{V_f} \tan \left[\frac{u(t-t_f)}{2L_e} \right]}{1 + \frac{V_f}{u} \tan \left[\frac{u(t-t_f)}{2L_e} \right]}, \quad (4.4)$$

where $u = (2\sigma/\rho R_n)^{1/2}$, t_f is the starting time for the integration, at point f , when the average velocity across the nozzle exit is $V_f = V_n(t_f)$.

Figure 6 compares $V_n(t)$ predicted from the simple one-dimensional model and the numerical solution of figure 5(a). At the start, the model slightly underestimates the rate of deceleration, probably because the velocity profile is not a perfect plug flow. Toward the end, however, it overestimates the deceleration as the capillary pressure at the exit falls below $2\sigma/R_n$ and approaches σ/R_n . Overall, the simple model captures reasonably well the evolution of V_n , which feeds the jet and determines whether auto-ejection occurs. In particular, note how L_e dictates the time scale of deceleration of V_n in (4.4). Physically, a larger L_e implies a longer liquid column moving with a greater kinetic energy. Thus, the deceleration will be slower, and a longer jet will probably be produced, in favour of auto-ejection. This point will be revisited in the next subsection. Finally, we have also confirmed that for the small Oh tested, viscous dissipation makes a very small contribution to the energy balance of (4.2), consistent with previous arguments on the unimportance of viscosity in the process.

4.2. Critical conditions for auto-ejection

Naturally, we think of a Weber number to represent the idea that the upward momentum must overcome the capillary restriction for auto-ejection to occur. However,

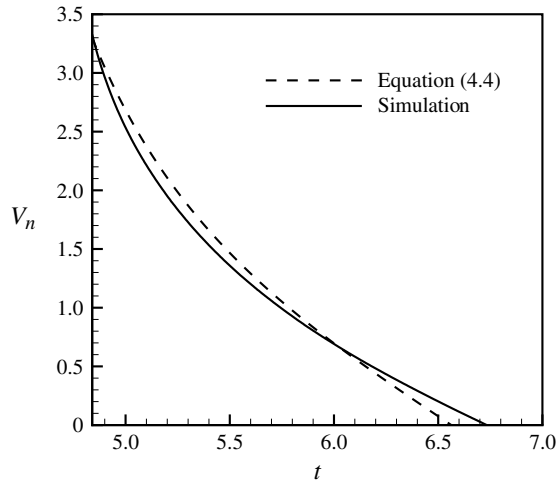


FIGURE 6. Temporal variation of the instantaneous velocity $V_n(t)$ at the nozzle exit, starting from point f at $t_f = 4.85$. The decline observed in the numerical simulation is well represented by a one-dimensional model based on energy conservation, (4.4).

there are two difficulties in constructing such a Weber number. First, there is no obvious characteristic velocity. The meniscus velocity is itself determined by the wicking inside the tube, and thus by the contact angle and geometry (especially length) of the tube and nozzle. It also changes in time and in space. Wollman & Weislogel (2013) suggested a nozzle Weber number defined using the liquid velocity at the exit of the nozzle when the meniscus first reaches that point. This corresponds to our point e in figure 5. Let us take this point as the nominal start of the ejection process $t^* = 0$, with $t^* = t - t_e$ measuring the time from this point onward. Using the velocity $V_e = V_n(t_e)$ at this point, we can define an instantaneous Weber number:

$$We = \frac{\rho V_e^2 R_n}{\sigma}. \quad (4.5)$$

Note that in the previous subsection, we have integrated (4.2) starting from point f , which is convenient for evaluating the capillary pressure and energy efflux. For defining the instantaneous Weber number, point e is more convenient as it is more clearly defined as the onset of contact line pinning at the nozzle exit.

Second, the instantaneous velocity V_e or We does not completely determine the fate of the jet and breakup. Figure 7(a) shows that We does not delineate sharply the boundaries separating non-pinch-off and pinch-off, nor among different numbers of droplets produced. Two capillary tubes of different lengths can produce the same instantaneous We at the nozzle exit, and yet very different outcomes of drop ejection. Figure 7(b) shows such an example. Under conditions that are otherwise identical to figure 5, a shorter capillary tube ($L = 1.5$) produces a short jet and no breakup, whereas the longer tube ($L = 5$) of figure 5 does lead to auto-ejection. The Weber number $We = 7$ is the same in both cases. Thus, the instantaneous Weber number We , by itself, is not adequate to predict the subsequent jet and drop dynamics outside the nozzle. This inadequacy is not hard to appreciate. As the jet issues from the nozzle, the kinetic energy of the liquid is being used to create a new air–liquid interface, and

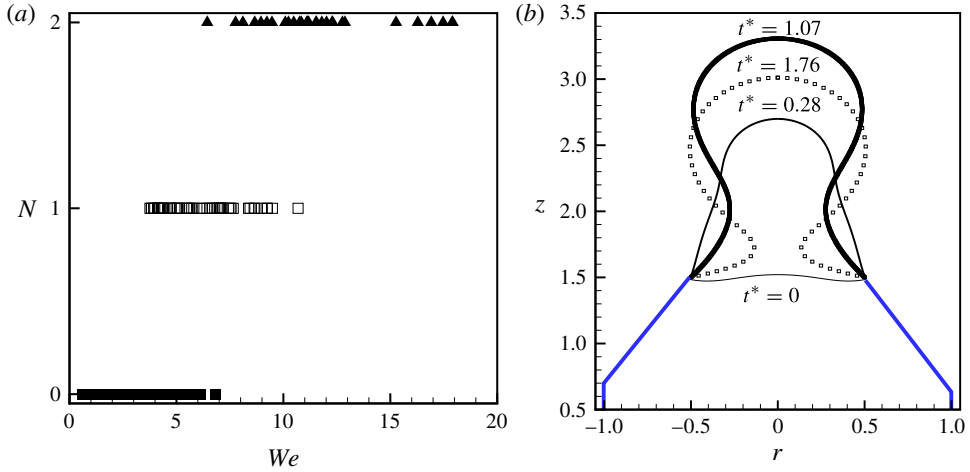


FIGURE 7. (Colour online) (a) Number of drops produced N as a function of We . The wide overlaps between different outcomes indicate that We does not provide an adequate criterion for auto-ejection of droplets. These data cover most of the parameter ranges studied: $0.005 \leq Oh \leq 0.02$, $0.25 \leq C \leq 1$, $1 \leq L \leq 10$ and $0 \leq \alpha \leq 40^\circ$. (b) A short tube ($L = 1.5$) fails to produce drop ejections under identical conditions to figure 5, where a longer tube ($L = 5$) does produce ejection. The jet reaches maximum length at $t^* = 1.07$ and then retracts.

the liquid velocity declines in time. Roughly speaking, the maximum length that the jet can attain is determined by converting the initial kinetic energy of the entire liquid column at $t^* = 0$ into liquid–air surface energy. Thus, the length of the liquid column should matter as much as We .

Since we have previously introduced an effective tube length L_e (4.3), it seems natural to use it, together with We , to account for the total amount of kinetic energy prior to jet formation. Figure 8 plots the outcome of jet breakup against two parameters, We and L_e , where L_e has been made dimensionless by R . The overlaps in the We plot (figure 7a) have now been clarified by L_e . This plot suggests the following critical conditions for predicting drop formation in auto-ejection:

$$N = \begin{cases} 0 & \text{if } We < 3.4f(L_e) \\ 1 & \text{if } 3.4f(L_e) < We < 5.5f(L_e) \\ 2 & \text{if } We > 5.5f(L_e) \end{cases} \quad (4.6)$$

where $f(L_e) = 1 + 0.8/L_e$. For the range of parameters tested here, ejection of three and more droplets has been observed mainly for large contraction angles, which produce a different flow regime to be considered in § 4.3. Thus we do not include these cases here.

A few remarks about (4.6) seem in order. First, the formula is general as it encompasses almost the entire parameter ranges explored in our simulations. The material and geometric parameters of the problem have been included through We and L_e . The only exception is large contraction angles α that induce additional flow patterns. These will be dealt with separately in § 4.3. Second, the critical condition for auto-ejection is in terms of We and L_e , and does not explicitly account

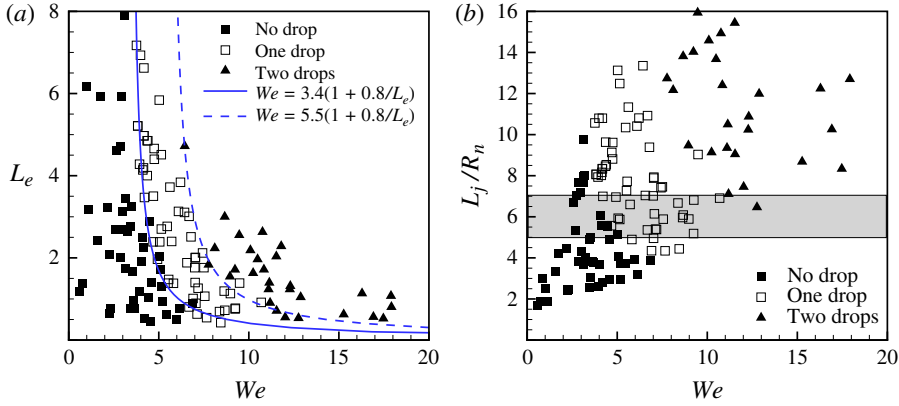


FIGURE 8. (Colour online) (a) Critical conditions for auto-ejection: number of droplets plotted as a function of We and the effective length L_e of (4.3). The three outcomes are demarcated by $We = 3.4(1 + 0.8/L_e)$ and $We = 5.5(1 + 0.8/L_e)$, shown as the solid and dashed curves, respectively. (b) The grey band, representing $5 \leq L_j/R_n \leq 7$ for the jet length of (4.7), indicates a rough threshold for auto-ejection.

for the jet dynamics outside the nozzle, including the process of end-pinching. This is because the dynamics outside the nozzle are in principle dictated by these two control parameters. More specifically, We indicates the instantaneous upward momentum of the liquid column before the jet is produced, and L_e governs how that momentum decays in time (cf. (4.4)). Taken together, they determine the ultimate length of the jet that can be produced, which in turn determines whether end-pinching occurs and how many drops result. Equating the kinetic energy and meniscus surface energy at $t^* = 0$ to the surface energy of a cylindrical jet of radius R_n , $(\pi/2)R_n^2\rho L_e V_e^2 + 2\pi R_n^2\sigma = 2\pi R_n L_j\sigma$, we estimate the eventual length of the jet L_j once the kinetic energy has been completely converted to surface energy:

$$L_j = \frac{We}{4}L_e + R_n. \quad (4.7)$$

Now the numerical results of figure 8(a) can be reinterpreted in terms of L_j in figure 8(b). Roughly speaking, the transition from non-ejection to ejection occurs over the range of $5 \leq L_j/R_n \leq 7$. This coincides with the critical jet length that Castrejón-Pita, Castrejón-Pita & Hutchings (2012b) determined for end-pinching on an initially stationary filament, $L_j/R_n = 6 \pm 1$. Thus L_j provides a connection between auto-ejection, in which the mass flux at the nozzle exit varies in time, and end-pinching on a stationary filament where that flux is nil. The correspondence is not perfect, of course, since our jet shape can differ considerably from a perfect cylinder. At small Weber numbers, the strong capillary force makes the shape of the jet more spherical. As a result, ejection only happens at higher value of L_j than that expected for a cylindrical jet. At high Weber numbers, the decelerating velocity V_n at the exit produces a conical jet shape with a tapering tip. This amounts to an effectively thinner jet diameter, and consequently a smaller critical aspect ratio L_j for breakup.

As a criterion, (4.6) is somewhat unsatisfactory in that it is expressed in terms of We based on the instantaneous velocity V_e , which is not one of the material or geometric

parameters but a complex function of them. We have found no straightforward way to model V_e . This is because the acceleration of the meniscus in the nozzle depends on the dynamic contact angle θ_d , which depends on the meniscus velocity in turn (cf. figure 4). In this work, therefore, we have to content ourselves with a threshold for auto-ejection in terms of an instantaneous Weber number, instead of a true criterion that can be evaluated from the material properties and the geometry. This is a disappointment since obtaining such a criterion has been a motivation for the present study.

The critical conditions appear consistent with the experimental data of Wollman & Weislogel (2013). These data were presented in terms of a Weber number at the exit, similar to our We except that the local velocity was estimated using scaling arguments. Similar to our figure 7(a), different outcomes overlap considerably in terms of We values. Non-ejection was observed for We from around 2 up to nearly 20. The ejection of one or two droplets occurred for $6 < We < 20$, while three or more drops were seen for We above 10. Since the geometric parameters were not reported for the individual data points, we are unable to compute L_e and use it to untangle the data as we have done in figure 8. Thus, we can only observe that the experimental data suggest threshold We values that are consistent with our results in figure 8.

Finally, (4.6) makes an interesting prediction about the impossibility of auto-ejection in a straight capillary tube. The maximum meniscus velocity in a straight capillary tube is the capillary–inertial velocity v_{ci} (1.1), which yields a Weber number $We = 2 \cos \theta_d \leq 2$. This is smaller than the minimum We for auto-ejection $We = 3.4f(L_e) > 3.4$. Thus, auto-ejection cannot occur in straight tubes, as has been suggested by empirical observations (Siegel 1961; Wollman & Weislogel 2013).

4.3. Rapid ejection and air entrapment

This subsection deals with two additional flow regimes encountered at large values of the contraction angle α . In constructing the pinch-off conditions of (4.6), we have encoded all geometric effects into L_e . The contraction induces an inward radial flow, one consequence of which is to increase the average velocity of the liquid and its total kinetic energy. Using a one-dimensional plug flow assumption, we have represented the acceleration effect in L_e . For larger contraction angles, however, the two-dimensional nature of the flow becomes important, and the radial flow tends to modify the meniscus shape and the dynamic contact angle, thus producing new regimes of interfacial breakup.

As a baseline, we take the simulation depicted in figure 5 at contraction angle $\alpha = 30^\circ$. In this simulation, when the contact line reaches the exit (point e), the meniscus as a whole arrives at the exit as well, with a more or less flat interface and uniform velocity profile (cf. figure 5c). Subsequently, a more or less cylindrical jet forms (point g), which grows to a maximum length around $5R_n$ before end-pinching produces a single drop with a diameter comparable to that of the nozzle. Considering this baseline scenario as ‘regular ejection’, we encounter two additional regimes at higher α , termed rapid ejection and air entrapment.

Rapid ejection is illustrated in figure 9 for $\alpha = 45^\circ$. The stronger contraction leads to faster acceleration of the contact-line speed as well as a larger and increasing contact angle. Since capillarity cannot keep up with the rapid contact-line movement, the meniscus deviates markedly from a spherical shape, and a deep depression forms in the centre (figure 9a, $t^* = 0$). Alternatively, one may note that as the meniscus enters the nozzle, the sudden change in wall orientation sends a capillary wave

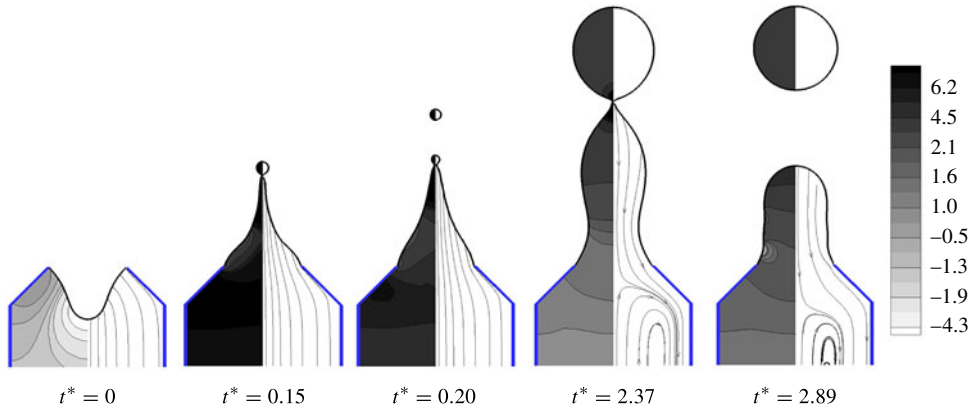


FIGURE 9. (Colour online) The regime of rapid ejection at contraction angle $\alpha = 45^\circ$, other conditions being identical to those in figure 5. The series of snapshots starts with contact-line pinning at the nozzle exit ($t^* = 0$), and shows ejection of the first, second and third drop before retraction of the filament ($t^* = 2.89$). The pressure contours are plotted in the left half of the domain while the streamlines are in the right half.

propagating radially inward. Then the interfacial depression may be viewed as due to the wavefront meeting at the centre. Afterwards, the strong radial flow converges toward the centre, while surface tension rapidly flattens the deeply curved interface. These two effects conspire to produce a high pressure at the nozzle exit and a highly non-uniform velocity profile when the meniscus as a whole reaches the exit. The centreline velocity is roughly 7 times the average velocity V_n at this moment, as compared with $1.2V_n$ in the baseline case. As a result, a thin, fast jet forms, at the tip of which the first drop is ejected quickly at $t^* = 0.15$, with a dimensionless drop radius $r = 0.07$ and velocity $v = 14.8$. This is followed by a second small drop ($r = 0.046$, $v = 6.9$) at $t^* = 0.2$, and a much larger third one ($r = 0.54$, $v = 0.06$) after a much longer interval at $t^* = 2.37$. By this time, the first two droplets have moved outside the computational domain. After the third drop, the jet retracts ($t^* = 2.89$). In contrast, the baseline case has its first and only ejection at $t^* = 1.66$, producing a larger and slower drop ($r = 0.61$, $v = 1.02$).

The regime of rapid ejection of figure 9 has been confirmed by experimental observations under microgravity (A. Wollman, private communication, 2013). Moreover, the regime is reminiscent of inkjet printing that uses a carefully controlled pressure pulse to eject fine droplets (Chen & Basaran 2002; Basaran & Xu 2012). But the underlying mechanisms are quite different. In our problem, it is the spatial variation of the liquid velocity that generates large local curvature and hence small droplets. In inkjet printing, on the other hand, it is a precise control of the timing of the forward and backward flows, with respect to the capillary time for drop formation, that limits the amount of liquid in the ejected drops.

In view of the rapid ejection of high-speed droplets, higher α may help induce auto-ejection under normal-gravity conditions. Indeed, the ancillary video of Wollman *et al.* (2012) depicts auto-ejection under normal gravity using a large contraction angle $\alpha \approx 50^\circ$ and $Bo = 0.26$. We have carried out a limited exploration of such scenarios, and an example is depicted in figure 10 for Bond number $Bo = \rho R^2 g / \sigma = 0.4$ at $\alpha = 50^\circ$. After the ejection of one droplet ($t^* = 0.34$), the jet grows a bulb at the tip while forming a neck at the base ($t^* = 0.42$). Shortly afterwards, the neck pinches

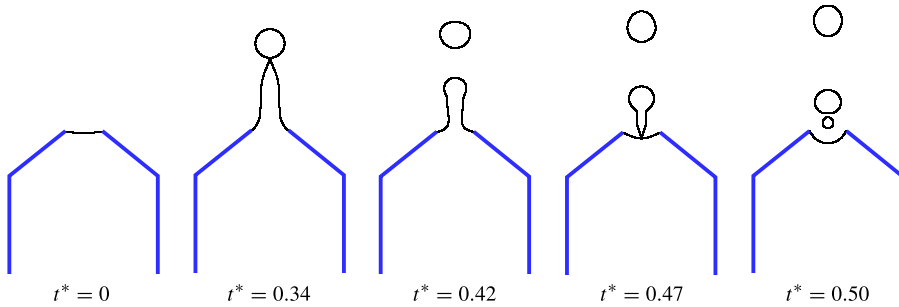


FIGURE 10. (Colour online) Auto-ejection under gravity for large contraction angle $\alpha = 50^\circ$. Here $Bo = 0.4$, $Oh = 0.01$, $C = 0.25$, $L = 2$. After ejecting a single droplet at $t^* = 0.34$, the jet pinches off at its base ($t^* = 0.47$), and later breaks up into two more drops ($t^* = 0.5$).

in and the bulb detaches ($t^* = 0.47$), producing two more drops of disparate size ($t^* = 0.5$). Under the same conditions, contraction angles below 40° do not produce auto-ejection at all. It is thanks to the stronger radial flow that a thin jet forms against gravity and breaks up into droplets.

Air entrapment occurs at an even larger contraction angle of $\alpha = 55^\circ$ (figure 11). At $t^* = 0$, the interface forms a depression as in the rapid-ejection regime. Subsequently, however, the radial flow is so strong as to cause the depression to narrow and deepen, producing an air finger. At $t^* = 0.08$, the neck of the air finger pinches off, entrapping a bubble in the liquid. Given the relatively short length of the air finger, the pinch-off is mainly driven dynamically by the inward liquid flow rather than interfacial tension as in Rayleigh–Plateau instability. After this, the strong momentum of the liquid continues to propel the jet forward, much like the later stage of figure 9. This leads to the ejection of a large drop ($r = 0.49$, $v = 0.71$) at $t^* = 1.68$. Eventually the jet retracts. Experimentally, Wollman *et al.* (2012) demonstrated the possibility of air entrapment at a contraction angle around 50° , providing direct evidence for this unusual flow regime.

Figure 11 exhibits two notable features rooted in the essence of the diffuse-interface model. One is the coalescence of the two surfaces at $t^* = 0.08$, and the other is the disappearance of the small entrapped air bubble between $t^* = 0.18$ and $t^* = 1.68$. Due to Cahn–Hilliard diffusion, nearby interfaces experience an attraction force similar to the van der Waals force (Yue *et al.* 2005; Yue, Zhou & Feng 2006). Thus, two interfaces merge naturally in diffuse-interface simulations. The diffusion across an interface may lead to shrinkage and even disappearance of a small drop or bubble, as the interface shifts slightly at the expense of the bulk energy, resulting in a lower total energy. A well-known manifestation of this diffusive mechanism is Ostwald ripening (Voorhees 1992). Given the time and length scales here, however, the dissolution of the bubble into the liquid is likely to be an artifact. Yue, Zhou & Feng (2007) have examined this process in detail. The shrinkage effect is particularly noticeable for a small domain of one phase enclosed in a large domain of the other. If the enclosed domain is large, shifting the phase-field parameter inside it becomes energetically prohibitive. Thus, the interface between the jet and the ambient air is little affected by interfacial diffusion.

For even larger values of α , the contraction obstructs much of the upward momentum of the liquid column. One possible outcome is the formation of a

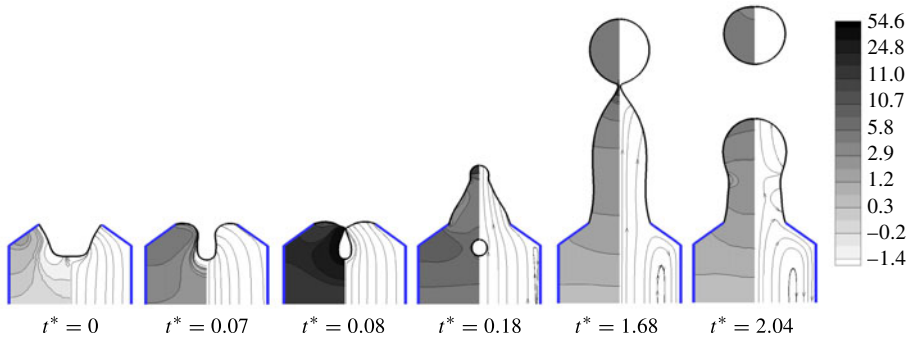


FIGURE 11. (Colour online) Air entrapment at contraction angle $\alpha = 55^\circ$, other conditions being identical to those in figure 5. The snapshots show pressure contours on the left and streamlines on the right. Strong inward radial flow produces an air finger at $t^* = 0.069$, which then pinches off at $t^* = 0.079$ to trap an air bubble in the liquid. The air bubble disappears later due to Cahn–Hilliard diffusion.

droplet with a small or zero upward velocity. If the momentum of the liquid column is relatively low to begin with, which occurs for a short tube length L or large contraction ratio C , drop ejection can be suppressed completely. Thus, auto-ejection favours an intermediate range of α values. Too gentle a contraction does not provide sufficient flow focusing to produce a long jet. Too abrupt a contraction stifles the momentum of the liquid column.

4.4. Contact-line de-pinning at the nozzle lip

So far, we have assumed the nozzle exit to be a horizontal surface of width W_l that is non-wettable by the liquid ($\theta_l = 180^\circ$). Thus, the contact line is pinned at the inner corner of the lip. Under certain experimental conditions, the contact line has been observed to de-pin and move outward (Wollman *et al.* 2012). This effectively broadens the base of the jet and changes the outcome of drop ejection (Ambravaneswaran *et al.* 2004). Such observations have motivated us to relax the pinning condition by imposing a smaller θ_l so that the effect of contact-line de-pinning can be investigated.

Figure 12 depicts the effect of contact-line de-pinning by tracking the position of the interface in time for several values of θ_l . As the jet emanates from the nozzle, the interfacial slope never exceeds 90° relative to the upper surface of the lip. Thus, for $\theta_l \geq 90^\circ$, the contact line remains pinned at the inner corner of the lip and θ_l has no effect. These cases are represented by the $\theta_l = 90^\circ$ curve in figure 12(a). The geometric and physical conditions for these runs correspond to $We = 6.9$ and $L_e = 1.54$, and thus auto-ejection of a single drop occurs according to figure 8. As θ_l reduces to 80 and 70° , the contact line de-pins and moves radially outward. This hampers the lengthening of the jet and delays the pinch-off (e.g. $\theta_l = 70^\circ$ curve). The drop produced is also somewhat larger. At the point of pinch-off, the contact line is somewhere on the flat part of the upper surface, not having reached the outer corner. For $\theta_l \leq 60^\circ$, the length of the jet is further stunted and drop ejection is completely suppressed. For these cases, the contact line reaches the outer edge of the lip and stays pinned there, at least until the jet retracts.

Figure 12(b) analyses the suppression of drop ejection for $\theta_l = 45^\circ$. De-pinning of the contact line at the inner corner of the lip takes place at point a when the

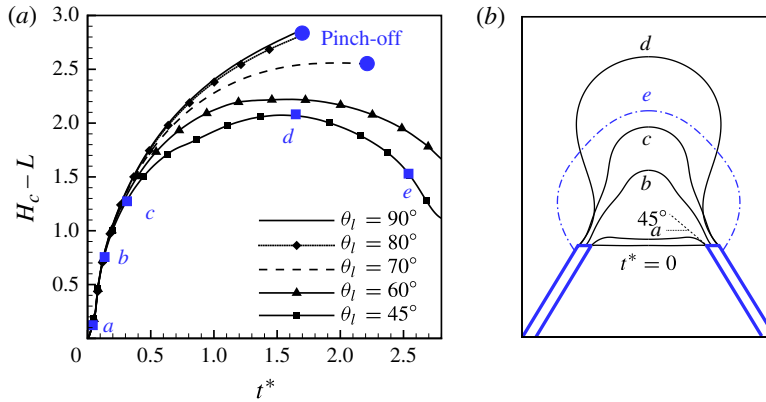


FIGURE 12. (Colour online) (a) Effect of contact-line de-pinning on the growth of the jet and drop ejection. The ordinate is the length of the jet measured from the exit of the nozzle, and the abscissa is time starting from the moment of the contact line reaching the inner corner of the lip. Drop pinch-off is indicated by a filled circle. The lip of the nozzle has a width $W_l = 0.25R_n$ and a static contact angle θ_l . The other parameters of the simulation are the same as in figure 5 except a shorter $L = 4$. (b) Snapshots of the interface for $\theta_l = 45^\circ$ at points marked on the curve.

interface makes an angle of 45° with respect to the upper surface of the exit. After de-pinning, the contact line moves radially outward, broadening the base of the jet. This reduces the upward liquid velocity through mass conservation. Moreover, the curvature of the meniscus is moderated (point b), resulting in a lower capillary pressure at the base of the jet. Both effects conspire to restrain the lengthening of the jet. The contact line reaches the outer corner of the lip at point c , and the jet length peaks at point d some time later. This maximum jet length, at $2R$ or $4R_n$ in this case (figure 12a), is approximately 25% shorter than the case without contact-line de-pinning ($\theta_l \geq 90^\circ$). It is too short for drop ejection (cf. figure 8b). Thus, the jet retracts and flattens afterwards, driving the contact line past the outer corner, producing the nearly spherical interface of point e .

Insofar as the contact line becomes pinned at the outer corner of the lip during the growth phase of the jet, the width W_l of the lip should also affect the jet behaviour. For a fixed $\theta_l = 45^\circ$, we have examined the effect of increasing W_l from $0.05R_n$ to $2R_n$ (figure 13). As expected, a wider lip broadens the base of the jet, inhibits the lengthening of the jet, and suppresses the potential for drop ejection.

5. Conclusions

As far as we know, this study represents the first numerical computation of the process of auto-ejection. In interpreting the numerical results, we have also developed simple models to describe various aspects of the process. The parameter range captures most of the experimental conditions, and we reproduce all the salient features of the experimental observations. The main results of the study can be summarized as follows.

- (a) At the start of imbibition, the meniscus quickly attains the capillary–inertial regime in the straight tube, and advances with a mostly constant velocity until it enters the contraction in the nozzle, where it accelerates. The dynamic contact

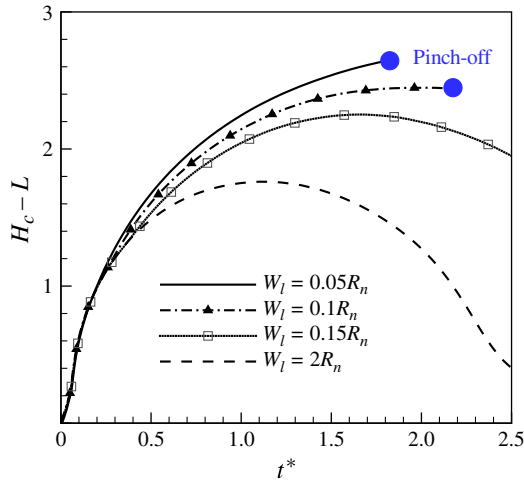


FIGURE 13. (Colour online) Effect of the width of the lip W_l on jet growth and drop ejection for $\theta_l = 45^\circ$. The other parameters are the same as in figure 12.

angle increases with the meniscus speed. Viscosity has a negligible role in the entire process.

- (b) With the contact line pinned at the inner corner of the exit, a jet issues into the ambient air. The lengthening of the jet is accompanied by deceleration of the liquid column inside the tube, with kinetic energy being converted into surface energy. An energy balance model captures the temporal decay of the liquid velocity at the nozzle quite accurately. This rate of decay is dictated by an effective length that embodies the geometric features of the tube–nozzle combination.
- (c) A two-parameter critical condition for auto-ejection of droplets is developed using the instantaneous Weber number when the contact line first arrives at the nozzle exit and the effective length. Together they determine the length of the jet that may be produced when the available kinetic energy is converted into surface energy. This critical length agrees with prior studies of end-pinching on an initially stationary filament, thus demonstrating auto-ejection as being rooted in essentially the same hydrodynamics.
- (d) With increasing contraction angle, we predict additional regimes of rapid ejection of multiple drops and air bubble entrapment. When the contraction is too mild, auto-ejection is suppressed. In particular, auto-ejection is impossible in a straight tube.
- (e) To the extent that comparisons can be made, the numerical results agree with experimental observations. In particular, the three regimes – regular auto-ejection, rapid ejection and bubble entrapment – have been observed in experiments.

It is interesting to note the host of factors that may suppress auto-ejection. Aside from the mild contraction angle noted above, the lip of the nozzle also plays a role. A more wettable and wider lip will hinder jet elongation and drop ejection. Gravity tends to suppress auto-ejection as well, although our results show that it may be compensated by a strong contraction. Viscosity plays a negligible role under typical experimental conditions, and is thus neglected in this study. But an increasing viscosity

will eventually retard the capillary rise and inhibit auto-ejection. With other conditions being fixed, there should exist a critical Ohnesorge number for auto-ejection. This has not been explored in the current study.

Another limitation of the study is that the critical condition for auto-ejection is given in terms of an instantaneous Weber number, rather than in terms of the material and geometric parameters. We attempted to model the instantaneous velocity at the nozzle in terms of these parameters, with little success. As compared with other microfluidic drop-forming procedures, auto-ejection is unique in that it involves no external force or flux, and is entirely autonomous. From this standpoint, it will be desirable to devote future work to developing a true criterion for auto-ejection in terms of the geometric and material parameters.

Acknowledgements

We thank A. Wollman for generously providing data and video of his experiments to us, and for useful discussions. The study was supported by NSERC, the Canada Research Chair program, and the Canada Foundation for Innovation. Part of the work was done while J.J.F. was a visitor at the Kavli Institute for Theoretical Physics, Santa Barbara, and he acknowledges support by the National Science Foundation (NSF PHY11-25915).

REFERENCES

- AMBRAVANESWARAN, B., SUBRAMANI, H. J., PHILLIPS, S. D. & BASARAN, O. A. 2004 Dripping-jetting transitions in a dripping faucet. *Phys. Rev. Lett.* **93**, 034501.
- AMBRAVANESWARAN, B., WILKES, E. D. & BASARAN, O. A. 2002 Drop formation from a capillary tube: comparison of one-dimensional and two-dimensional analyses and occurrence of satellite drops. *Phys. Fluids* **14**, 2606–2621.
- ANNA, S. L., BOUTOUX, N. & STONE, H. A. 2003 Formation of dispersions using flow focusing in microchannels. *Appl. Phys. Lett.* **82**, 364–366.
- ANTKOWIAK, A., BREMOND, N., DUPLAT, J., LE DIZÈS, S. & VILLERMAUX, E. 2007 Cavity jets. *Phys. Fluids* **19**, 091112.
- BASARAN, O. A., GAO, H. & BHAT, P. P. 2013 Nonstandard inkjets. *Annu. Rev. Fluid Mech.* **45**, 85–113.
- BASARAN, O. & XU, Q. 2012 Method for producing ultra-small drops. US Patent 8,186,790.
- BOSANQUET, C. H. 1923 On the flow of liquids into capillary tubes. *Philos. Mag.* (6) **45**, 525–531.
- BRACKE, M., DE VOEGHT, F. & JOOS, P. 1989 The kinetics of wetting: the dynamic contact angle. *Prog. Colloid Polym. Sci.* **79**, 142–149.
- CASTREJÓN-PITA, J. R., CASTREJÓN-PITA, A. A., HINCH, E. J., LISTER, J. R. & HUTCHINGS, I. M. 2012a Self-similar breakup of near-inviscid liquids. *Phys. Rev. E* **86**, 015301.
- CASTREJÓN-PITA, A. A., CASTREJÓN-PITA, J. R. & HUTCHINGS, I. M. 2012b Breakup of liquid filaments. *Phys. Rev. Lett.* **108**, 074506.
- CHEN, A. U. & BASARAN, O. A. 2002 A new method for significantly reducing drop radius without reducing nozzle radius in drop-on-demand drop production. *Phys. Fluids* **14**, L1–L4.
- DONG, H., CARR, W. W. & MORRIS, J. F. 2006 An experimental study of drop-on-demand drop formation. *Phys. Fluids* **18**, 072102.
- GAO, P. & FENG, J. J. 2009 Enhanced slip on a patterned substrate due to depinning of contact line. *Phys. Fluids* **21**, 102102.
- GAO, P. & FENG, J. J. 2011 A numerical investigation of the propulsion of water walkers. *J. Fluid Mech.* **668**, 363–383.
- GEKLE, S. & GORDILLO, J. M. 2010 Generation and breakup of Worthington jets after cavity collapse. Part 1. Jet formation. *J. Fluid Mech.* **663**, 293–330.

- GOLDMANN, T. & GONZALEZ, J. 2000 DNA-printing: utilization of a standard inkjet printer for the transfer of nucleic acids to solid supports. *J. Biochem. Biophys. Meth.* **42**, 105–110.
- GORDILLO, J. M. & GEKLE, S. 2010 Generation and breakup of Worthington jets after cavity collapse. Part 2. Tip breakup of stretched jets. *J. Fluid Mech.* **663**, 331–346.
- HA, J. & LEAL, L. G. 2001 An experimental study of drop deformation and breakup in extensional flow at high capillary number. *Phys. Fluids* **13**, 1568–1576.
- HOFFMAN, R. L. 1975 A study of the advancing interface. I. Interface shape in liquid-gas systems. *J. Colloid Interface Sci.* **50** (2), 228–241.
- HUH, E. & SCRIVEN, L. E. 1971 Hydrodynamic model of steady movement of a solid/liquid/fluid contact line. *J. Colloid Interface Sci.* **35**, 85–101.
- JACQUIN, D. 2000 Contact-line dynamics of a diffuse fluid interface. *J. Fluid Mech.* **402**, 57–67.
- JIANG, T.-S., SOO-GUN, O.-H. & SLATTERY, J. C. 1979 Correlation for dynamic contact angle. *J. Colloid Interface Sci.* **69**, 74–77.
- LEIB, S. & GOLDSTEIN, M. 1986 Convective and absolute instability of a viscous liquid jet. *Phys. Fluids* **29**, 952–954.
- LOWNDES, J. 1980 The numerical simulation of the steady movement of a fluid meniscus in a capillary tube. *J. Fluid Mech.* **101**, 631–646.
- LUCAS, R. 1918 Ueber das Zeitgesetz des Kapillaren Aufstiegs von Flüssigkeiten. *Kolloid. Z.* **23**, 15–22.
- MARSH, J. A., GAROFF, S. & DUSSAN, V. 1993 Dynamic contact angles and hydrodynamics near a moving contact line. *Phys. Rev. Lett.* **70**, 2778–2781.
- MEHRABIAN, H. & FENG, J. J. 2011 Wicking flow through microchannels. *Phys. Fluids* **23**, 122108.
- NOTZ, P. K. & BASARAN, O. A. 2004 Dynamics and breakup of a contracting liquid filament. *J. Fluid Mech.* **512**, 223–256.
- QIAN, T., WANG, X.-P. & SHENG, P. 2006 A variational approach to moving contact line hydrodynamics. *J. Fluid Mech.* **564**, 333–360.
- QUÉRÉ, D., RAPHAËL, É. & OLLITRAULT, J. 1999 Rebounds in a capillary tube. *Langmuir* **15**, 3679–3682.
- SCHULKES, R. M. S. M. 1996 The contraction of liquid filaments. *J. Fluid Mech.* **309**, 277–300.
- SIBLEY, D. N., NOLD, A. & KALLIADASIS, S. 2013 Unifying binary fluid diffuse-interface models in the sharp-interface limit. *J. Fluid Mech.* **736**, 5–43.
- SIEGEL, R. 1961 Transient capillary rise in reduced and zero-gravity fields. *J. Appl. Mech.* **28**, 165–170.
- STANGE, M., DREYER, M. E. & RATH, H. J. 2003 Capillary driven flow in circular cylindrical tubes. *Phys. Fluids* **15**, 2587–2601.
- STONE, H. A. & LEAL, L. G. 1989 Relaxation and breakup of an initially extended drop in an otherwise quiescent fluid. *J. Fluid Mech.* **198**, 399–427.
- SUI, Y., DING, H. & SPELT, P. D. M. 2014 Numerical simulations of flows with moving contact lines. *Annu. Rev. Fluid Mech.* **46**, 97–119.
- SZEKELY, J., NEUMANN, A. W. & CHUANG, Y. K. 1971 The rate of capillary penetration and the applicability of the Washburn equation. *J. Colloid Interface Sci.* **35**, 273–278.
- TAKEUCHI, S., GARSTECKI, P., WEIBEL, D. B. & WHITESIDES, G. M. 2005 An axisymmetric flow-focusing microfluidic device. *Adv. Mater.* **17**, 1067–1072.
- TONG, A. Y. & WANG, Z. 2007 Relaxation dynamics of a free elongated liquid ligament. *Phys. Fluids* **19**, 092101.
- UMEMURA, A. 2011 Self-destabilizing mechanism of a laminar inviscid liquid jet issuing from a circular nozzle. *Phys. Rev. E* **83**, 046307.
- UTADA, A. S., LORENCEAU, E., LINK, D. R., KAPLAN, P. D., STONE, H. A. & WEITZ, D. A. 2005 Monodisperse double emulsions generated from a microcapillary device. *Science* **308**, 537–541.
- VOORHEES, P. W. 1992 Ostwald ripening of two-phase mixtures. *Annu. Rev. Mater. Sci.* **22**, 197–215.
- WASHBURN, E. W. 1921 The dynamics of capillary flow. *Phys. Rev.* **17**, 273–283.
- WILKES, E. D. & BASARAN, O. A. 2001 Drop ejection from an oscillating rod. *J. Colloid Interface Sci.* **242**, 180–201.

- WOLLMAN, A. 2012 Capillarity-driven droplet ejection. Master's thesis, Portland State University, USA.
- WOLLMAN, A., SNYDER, T., PETTIT, D. & WEISLOGEL, M. 2012 Spontaneous capillarity-driven droplet ejection. [arXiv:1209.3999](https://arxiv.org/abs/1209.3999) [physics.flu-dyn].
- WOLLMAN, A. & WEISLOGEL, M. 2013 New investigations in capillary fluidics using a drop tower. *Exp. Fluids* **54**, 1–13.
- XU, Q. & BASARAN, O. A. 2007 Computational analysis of drop-on-demand drop formation. *Phys. Fluids* **19**, 102111.
- YUE, P. & FENG, J. J. 2011a Can diffuse-interface models quantitatively describe moving contact lines? *Eur. Phys. J. - Spec. Top.* **197**, 37–46.
- YUE, P. & FENG, J. J. 2011b Wall energy relaxation in the Cahn–Hilliard model for moving contact lines. *Phys. Fluids* **23**, 012106.
- YUE, P., FENG, J. J., LIU, C. & SHEN, J. 2005 Diffuse-interface simulations of drop coalescence and retraction in viscoelastic fluids. *J. Non-Newtonian Fluid Mech.* **129**, 163–176.
- YUE, P., ZHOU, C. & FENG, J. J. 2006 A computational study of the coalescence between a drop and an interface in Newtonian and viscoelastic fluids. *Phys. Fluids* **18**, 102102.
- YUE, P., ZHOU, C. & FENG, J. J. 2007 Spontaneous shrinkage of drops and mass conservation in phase-field simulations. *J. Comput. Phys.* **223**, 1–9.
- YUE, P., ZHOU, C. & FENG, J. J. 2010 Sharp interface limit of the Cahn–Hilliard model for moving contact lines. *J. Fluid Mech.* **645**, 279–294.
- ZHOU, C., YUE, P. & FENG, J. J. 2006 Formation of simple and compound drops in microfluidic devices. *Phys. Fluids* **18**, 092105.
- ZHOU, C., YUE, P., FENG, J. J., OLLIVIER-GOOCH, C. F. & HU, H. H. 2010 3D phase-field simulations of interfacial dynamics in Newtonian and viscoelastic fluids. *J. Comput. Phys.* **229**, 498–511.